Microstructure of Multi-Pass Friction-Stir-Processed Al-Zn-Mg-Cu Alloys Reinforced by Nano-Sized TiB2 Particles and the Effect of T6 Heat Treatment

Xiaofei Ju, Fengguo Zhang, Zhe Chen, Gang Ji, Mingliang Wang, Yi Wu, Shengyi Zhong, Haowei Wang

metals

MDPI

Article

Microstructure of Multi-Pass Friction-Stir-Processed Al-Zn-Mg-Cu Alloys Reinforced by Nano-Sized TiB_2 Particles and the Effect of T6 Heat Treatment

Xiaofei Ju [1], Fengguo Zhang [1], Zhe Chen [1,*], Gang Ji [2], Mingliang Wang [3], Yi Wu [3,*], Shengyi Zhong [3] and Haowei Wang [1]

1 State Key Laboratory of Metal Matrix Composites, Shanghai Jiao Tong University, Shanghai 200240, China; juxiaofei211@sjtu.edu.cn (X.J.); fg.zhang@sjtu.edu.cn (F.Z.); hwwang@sjtu.edu.cn (H.W.)

2 Unité Matériaux et Transformations, CNRS UMR 8207, Université Lille 1, Villeneuve d'Ascq 59655, France; gang.ji@univ-lille1.fr

3 School of Materials Science and Engineering, Shanghai Jiao Tong University, Shanghai 200240, China; mingliang.wang@sjtu.edu.cn (M.W.); shengyi.zhong@sjtu.edu.cn (S.Z.)

* Correspondence: zhe.chen@sjtu.edu.cn (Z.C.); eagle51@sjtu.edu.cn (Y.W.); Tel.: +86-021-5474-7597 (Z.C.); +86-021-3424-2534 (Y.W.)

Received: 23 October 2017; Accepted: 14 November 2017; Published: 27 November 2017

Abstract: In this work, a fine-grained structure with a uniform distribution of TiB_2 particles and precipitates was achieved in TiB_2 particle-reinforced (PR) Al-Zn-Mg-Cu alloys by friction stir processing (FSP). The effects of multi-pass FSP on the microstructure, and TiB_2 particle distribution, as well as the microstructural evolution in the following T6 treatment, were investigated by X-ray diffraction, scanning electron microscopy and associated electron backscattered diffraction. The results showed that the distribution of TiB_2 particles and alloy precipitates was further improved with an increase in the FSP passes. Moreover, compared with alloy segregation in the as-cast PR alloys during T6 treatment, a complete solution of the precipitates was achieved in the FSP-treated PR alloys. The fine-grained structure of the FSP-treated PR alloys was thermally stable without any abnormal growth at the high temperature of T6 treatment due to the pinning effect of dispersed TiB_2 particles. The strength and ductility of the PR alloys were simultaneously improved by the combination of FSP and T6 treatment.

Keywords: friction stir processing; PR-aluminum alloy; nano-sized TiB_2 particles; thermal stability; T6 treatment

1. Introduction

In the past decades, in order to improve the mechanical properties of aluminum alloys, nano-sized ceramic particles such as TiB_2, SiC_p [1] and TiC [2] have been introduced to alloy matrixes as reinforcements to fabricate nano-particulate-reinforced alloy matrix composites. Especially by reducing the reinforcement particle size to the nanometer range, it has been reported that the tensile ductility of such PR alloys can be maintained or even enhanced with a simultaneous increase in tensile strength, depending on the processing process [3–5]. However, casting (i.e., liquid-state solidification) generally weakens ductility and toughness due to defects like porosity, particle-matrix debonding, and especially particle clustering [6]. Even the most vigorous stirring techniques like ultrasonic dispersion during casting are unable to break the agglomerates in the melt [7], which are pushed by the solidification front and ultimately cluster along the grain boundaries in the following solidification [8,9]. It is thus very tough work to distribute nanoparticles uniformly in the metal matrix [7]. Previous studies show that the particle clusters further have a negative effect on the solution treatment. For example, Hong et al. [10] studied TiB_2/2009 composites and found that the presence of nanoparticle clusters

inhibits the effective diffusion of alloy elements in the matrix, resulting in an insufficient solution. Geng et al. [11] increased the solution temperature of TiB_2/2024 Al composite and obtained little enhancement in the mechanical properties. As a result, the partial solution of the alloy phase in the cast PR alloys caused by particle clusters significantly reduces the response of age hardening.

FSP, as a severe plastic deformation technique (SPD), has been proved to be one of the most efficient ways for microstructural modification in the solid-state [12]. It can effectively solve the above-mentioned problems of cast defects and particle clusters in PR alloys [6,13]. In addition, FSP is regarded as a promising grain refinement technique [14–17]. However, microstructural instability at elevated temperatures is found to be a crucial problem in aluminum alloys with a fine grain size [18,19], thus the improvement of the final strength of those alloys is limited [20,21]. For example, Moradi et al. [22] studied the AA6061-AA2024 friction stir welding butt joint and found that abnormal grain growth occurred in the nugget zone. Regarding this, most of the research on FSP-treated aluminum alloys focused on non-heat-treatable alloys such as Al-Mg alloy [23,24]. The application of FSP to high-strength Al-Zn-Mg-Cu alloys has been reported in the past years [8,25,26]. However, their mechanical properties are not satisfactory due to the dilemma of fine grain size and solution treatment. In the present study, the effect of the FSP and the following T6 treatment on the microstructure and mechanical properties of heat-treatable Al-Zn-Mg-Cu alloys reinforced by nano-scaled TiB_2 particles is studied. The aims of this study are: (a) to examine the effect of particle distribution on the T6 solution treatment of PR alloys; (b) to evaluate the thermal stability of the FSP-treated PR alloys after T6 treatment; and (c) to investigate the relationship between the mechanical properties and the various microstructures processed by the combination of multi-pass FSP and T6 treatment.

2. Experiments

The TiB_2/Al-Zn-Mg-Cu composites with 3 vol. % of TiB_2 particles were fabricated by the in-situ mixed-salt method as reported in [27]. The in-situ grown TiB_2 particles in the Al matrix show a wide size distribution and most of them are nano-sized (<100 nm) [28]. Plates with the dimensions of 200 mm × 100 mm and a thickness of 16 mm were cut from the direct chilling cast ingot and followed by conventional homogenization. In this study, a taper round-screwed stir rod was used and made of H13 steel, with the dimensions of ∅6 (top)/∅8 (root) × 8 mm. FSP was performed on the plates with a tool rotation rate of 600 rpm, a traverse speed of 80 mm/min, a processing depth of 8 mm and a tool tilt angle of 2.5°. For multiple-pass FSP, the pin tool was traversed along the same line back and forth.

Microstructure characterization was done on the as-cast, as-produced FSP-treated samples and T6-treated FSP-treated samples. The T6 treatment contains two stages. Firstly, the samples were solutionized in an air furnace (Nabertherm, Lilienthal, Germany) at 475 °C for 70 m and quenched in water. Secondly, aging treatment was applied to the samples at 120 °C for 20 h. The FSP-processed samples were sectioned in the center of the nugget zone on the transverse plane and all the microstructural examinations were done on those cross sections. X-ray diffraction (XRD) (Rigaku, Tokyo, Japan) was utilized to determine the phases present in the samples and the measurements were performed on the Ultima IV by using monochromatic Cu K_α radiation. Scanning electron microscopy (SEM) (Tescan, Brno, Czech Republic) and energy dispersive spectroscopy (EDS) (Tescan, Brno, Czech Republic) were used to study the distribution of TiB_2 particles and alloy precipitates in the nugget zone and the as-cast PR alloys. The metallographic specimens were mechanically polished up to 0.05 μm with colloidal silica, while electron backscattered diffraction (EBSD) samples were prepared by mechanical and electrolytic polishing. Images and EBSD orientation maps were obtained using a TESCAN MAIA3 model 2016 instrument (Tescan, Brno, Czech Republic), operated at 20 kV, and interfaced to a BUEHLER QUANTAX EBSD system. A step size of 0.12 μm was set to consider the fine grains. The EBSD Kikuchi patterns were post-treated using CHANNEL 5.0 software (CHANNEL 5.0, Oxford Instruments, Oxford, UK) to determine the average grain sizes, grain aspect ratios, boundary misorientation distributions and the fraction of high angle grain boundary (HAGB) area. Boundaries with misorientation angles between 2° and 15° were defined as low angle

grain boundaries (LAGB), while those higher than 15° were defined as HAGB. In addition, boundaries with misorientation angles lower than 2° were not considered.

To evaluate the mechanical properties, dog-bone-shaped tensile specimens with a gage length of 15 mm and a width of 3 mm were cut from the as-cast PR alloys and the nugget zone along the FSP direction. These specimens were subsequently ground and polished to a final thickness of ~2 mm. Tensile tests were conducted on a Zwick/Roell Z100 machine (Zwick, UlM, Germany) at a constant strain rate of 10^{-3} s^{-1}. After tests, the failed specimens were subjected to fractographic examinations with SEM.

3. Results and Discussion

3.1. Microstructure of the As-Cast PR Alloy Samples

Figure 1a shows the SEM image of the as-cast PR alloy sample. The typical microstructure of the as-cast PR alloy shows equiaxed grains with an average grain size of about 27 μm, embedded in a network-like structure with light grey contrasts. According to the EDS map scanning in Figure 1b–f, the network-like areas are the clusters of TiB_2 particles on the micrometer scale with alloy segregation rich in Mg, Zn and Cu elements. This inhomogeneous distribution of particles derives from solidification [29], when particles are either engulfed or pushed by the advancing solid–liquid interface. At the same time, alloy segregation occurs with the clustering of ceramic particles during solidification, resulting in a very heterogeneous, network-like microstructure. Some very large particle clusters are also observed as marked by an arrow in Figure 1. The high magnification SEM images and EDS maps of the as-cast PR alloy sample before (Figure 2a–d) and after conventional T6 treatment (Figure 2e–h) are shown in Figure 2. According to the EDS map scanning, it can be clearly observed that alloy segregation rich in Cu and Mg elements remains near the TiB_2 clusters after conventional T6 treatment. Less Zn segregation is observed in Figure 2h. This phenomenon may be due to the different diffusion rates of the alloy elements. Deng et al. [30] studied the intermetallic phase evolution of 7050 Al during homogenization and found that the diffusion velocity of Zn was higher than that of Mg and Cu. The intermetallic phases in the as-cast PR alloys are difficult to dissolve during solution treatment. This is because the aggregated TiB_2 particles along the grain boundaries act as shells of the alloy segregation, which block most diffusion paths between the intermetallic particles and the matrix [10].

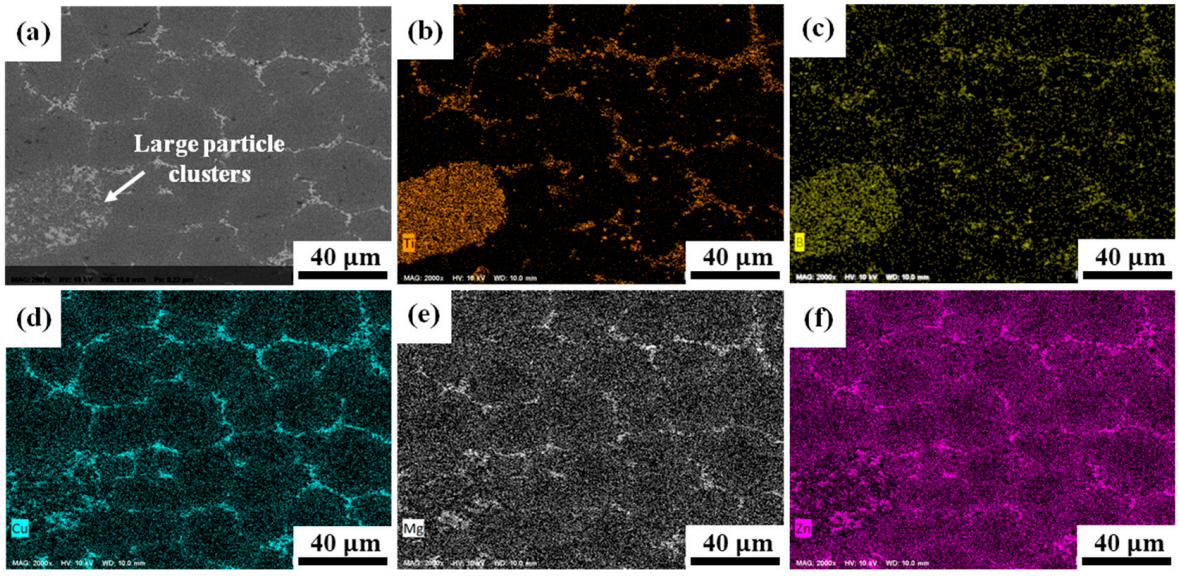

Figure 1. (**a**) Scanning electron microscopy (SEM) images of the as-cast particle-reinforced (PR) alloy sample; (**b**) corresponding energy dispersive spectroscopy (EDS) map scanning of Ti; (**c**) map scanning of B; (**d**) map scanning of Cu; (**e**) map scanning of Mg and (**f**) map scanning of Zn.

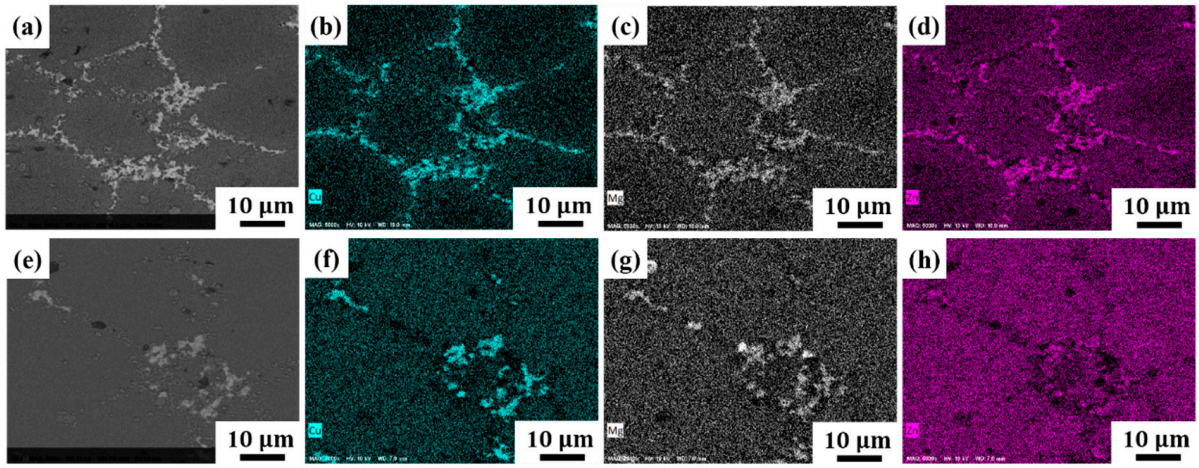

Figure 2. (**a**) SEM images of the as-cast PR alloy sample at higher magnification; (**b**) corresponding EDS map scanning of Cu; (**c**) map scanning of Mg; (**d**) map scanning of Zn; (**e**) SEM image of the T6-treated as-cast PR alloy sample at higher magnification; (**f**) corresponding EDS map scanning of Cu; (**g**) map scanning of Mg and (**h**) map scanning of Zn.

3.2. Microstructure of the FSP-Treated PR Alloy Samples

3.2.1. X-ray Diffraction Characterization

The XRD patterns of the as-cast and FSP-treated samples processed with various passes are presented in Figure 3. The XRD results reveal clearly the presence of TiB_2 phase in both the as-cast and FSP-treated samples, according to the Joint Committee on Powder Diffraction Standards (JCPDS): 35-0741. The alloy phases in the as-cast PR alloy are very complex, and may be $Al_2Mg_3Zn_3$ [31], Al_2CuMg [32,33], Al_2Cu [32], $MgZn_2$ [30]. As a result, these alloy phases are marked as $Al_xCu_xMg_xZn_x$ in the XRD pattern. The peaks of the $MgZn_2$ phase are observed clearly in the FSP-treated samples according to JCPDS: 34-0457. No diffraction peaks of intermetallics (such as Al_3Ti and AlB_2) and reaction residual salt (KBF_4) are detected in the PR alloys. The peaks of $MgZn_2$ are weak in the one-pass specimens, but become more obvious in the four-pass specimens. In the classical precipitation sequence of Al-Zn-Mg-Cu alloys, the precipitates vary from GP zones to η ($MgZn_2$) according to the aging temperature [34]. During FSP, the peak temperatures in different regions vary from 190 to 480 °C [12], which leads to the precipitation evolution. Su et al. [35] studied the Al-Zn-Mg-Cu alloy processed by friction stir welding and reported that η was the main precipitate in the stirring zone. A similar phenomenon was observed in the present study, in which the XRD patterns of the FSP-treated samples show the peaks of $MgZn_2$ and more $MgZn_2$ precipitates in the PR alloys with the increase of FSP passes.

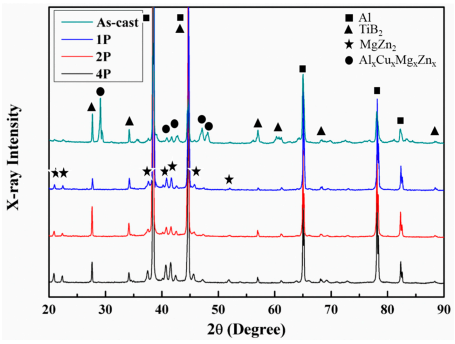

Figure 3. X-ray diffraction patterns for the as-cast and friction stir processing (FSP)-treated samples with various passes (1P, 2P and 4P represent 1-pass, 2-pass and 4-pass, respectively).

3.2.2. TiB_2 Distributions Characterized by Scanning Electron Microscopy

Figure 4 shows the SEM images of the nugget zone in the FSP-treated PR alloys processed with different passes. It can be clearly seen that TiB_2 particles disperse in the matrix without any particle cluster in all the FSP-treated samples. Compared with the large particle clusters in the as-cast PR alloys (Figure 1a), the dispersion of TiB_2 particles in the FSP-treated samples shows that FSP is an effective way to break clusters in PR alloys. This likely due to the SPD at high temperature during FSP, which softens the material and leads to the redistribution of the reinforcement particles [12]. However, as shown in Figure 4a, nonuniform TiB_2 distribution with a particle-rich zone and a particle-lean zone is evident in the one-pass FSP-treated PR alloys. With the increase in the processing passes, no particle-rich or -lean zone is observed and a more uniform TiB_2 distribution is obtained, as indicated in Figure 4b,c. This observation is consistent with the results of Huang et al. [6] and Zhang et al. [36], namely that multi-pass FSP improves the distribution of second-phase particles in an aluminum matrix due to the accumulated plastic strain. In addition, some TiB_2 particles are broken into several fragments as indicated by arrows in Figure 4a. This is probably related to the powerful stirring effect of the pin and the ensued severe plastic strain during FSP [37].

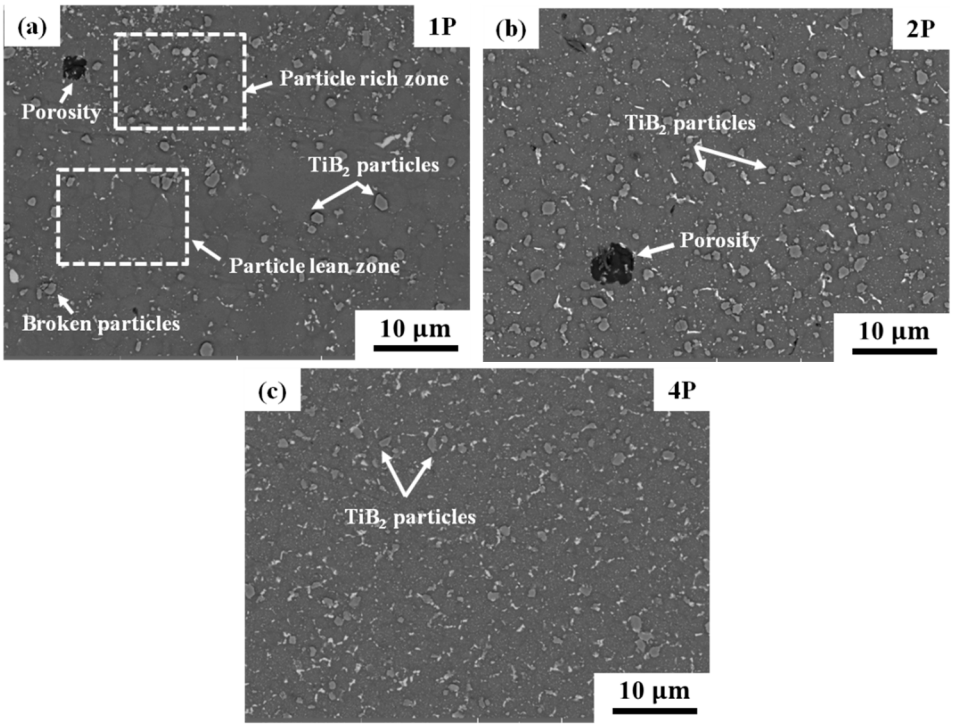

Figure 4. SEM images of the nugget zone in the FSP-treated PR alloys with (**a**) 1-pass; (**b**) 2-pass and (**c**) 4-pass.

3.2.3. Alloy Element Distributions Characterized by SEM/EDS

The SEM image and the corresponding EDS maps of the nugget zone in four-pass FSP PR alloys are shown in Figure 5. Fine and strip-like phases with bright, white contrasts are observed. According to the EDS maps shown in Figure 5d–f, these bright, white phases contain Cu, Mg and Zn elements and spread uniformly in the matrix. Both the aggregation of alloy elements and the TiB_2 clusters observed in Figure 1 are broken by the intense plastic strain and spread into the matrix with the material flow during FSP. As reported in [38], the temperature in the nugget zone can reach as high as 400–480 °C. Thus, the alloy phases will go into solution at such a high temperature and re-precipitate along the grain boundaries and on second phase particles [35,39]. This is consistent with the observation that the large, strip-like alloy phases are inclined to be located at grain boundaries, while some are situated

near or even overlapped with TiB_2 particles (as marked by arrows in Figure 6). As the number of FSP passes increases, the quantity of the precipitates is significantly raised, as shown in the XRD patterns of Figure 3. This phenomenon is also observed in FSP-processed 7075 aluminum alloy [40]. The increase in the quantity of precipitates with the addition of FSP passes is attributed to the multiplication of dislocations in the matrix. Since a more uniform particle distribution is introduced by multi-pass FSP, more interfaces between the particles and matrix are produced. During FSP, more dislocations are inclined to be produced from such interfaces [6]. The high dislocation density in the matrix induces the occurrence of pipe diffusion [41] and leads to the acceleration of the precipitating kinetic [15]. Therefore, the nucleation and growth of the precipitates are promoted and more precipitates are detected in the four-pass samples.

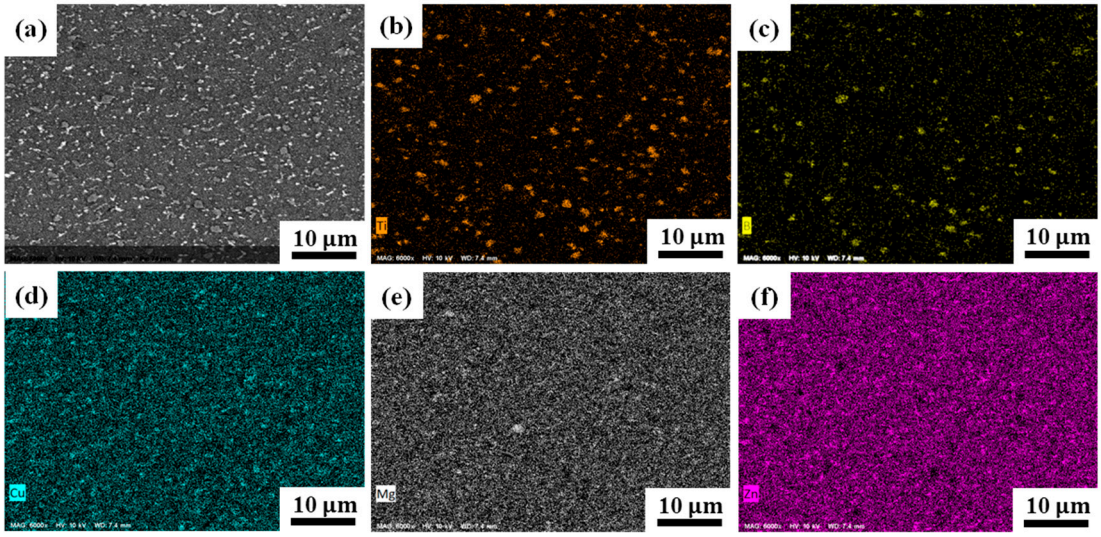

Figure 5. (**a**) SEM image of the nugget zone in the FSP PR alloy sample; (**b**) corresponding EDS map scanning of Ti; (**c**) map scanning of B; (**d**) map scanning of Cu; (**e**) map scanning of Mg and (**f**) map scanning of Zn.

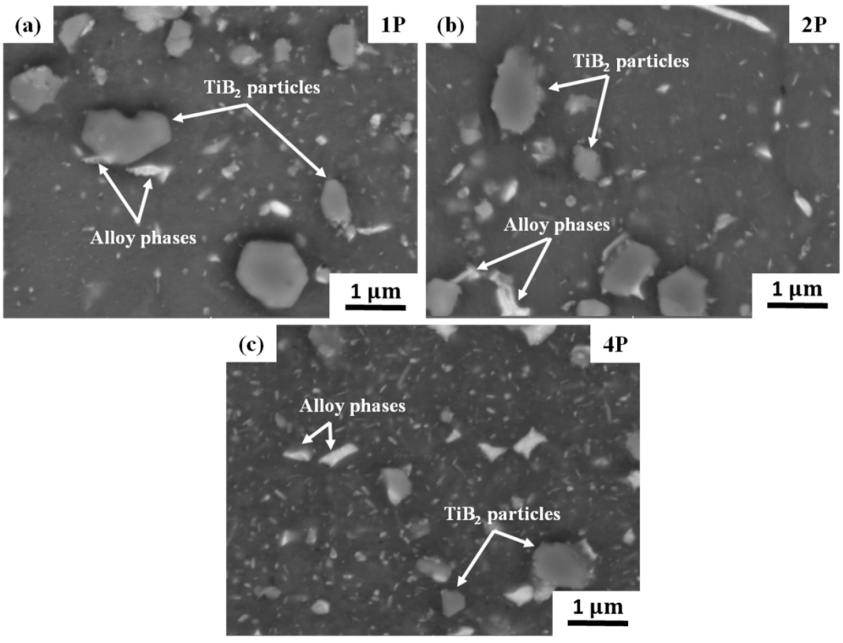

Figure 6. SEM images of the nugget zone in the FSP-treated PR alloys at higher magnification with (**a**) 1-pass; (**b**) 2-pass and (**c**) 4-pass.

3.2.4. Grain Size and Misorientation Distributions Characterized by EBSD

Figure 7 shows the orientation image microscopy (OIM) maps of the multi-pass FSP-treated PR alloys and the corresponding distribution of grain size and misorientation. The high-angle (> 15°) and low-angle grain boundaries (2–15°) are marked in black and green in the OIM maps, respectively. The white areas mainly along the grain boundaries are the zero resolution points. These areas encompass TiB_2 particles and alloy segregation that can hardly be detected by EBSD, due to their complex phase structures, enormous phase boundaries and accumulation of dislocations, etc. It can be seen that these undetected areas become smaller and more dispersed as the FSP passes increase. This phenomenon is consistent with the distribution of phases in multi-pass, FSP-treated samples (Figure 4). As shown in Figure 7a–c, a microstructure with a uniform and fine grain size distribution is obtained by FSP. Besides, the average aspect ratios of the grains are around one, as listed in Table 1, which implies that the grains are equiaxed. According to the statistics listed in Table 1, the average grain size of the FSP-treated PR alloys is in the range of 2–3 μm, which is one order of magnitude smaller than that of the as-cast PR alloys (around 27 μm). The obvious grain refinement in the stirring zone is the result of the complex effect of plastic deformation, dynamic recovery, continuous dynamic recrystallization and discontinuous dynamic recrystallization during FSP [42]. Besides, the addition of the nano-sized reinforced particles can lead to a fine grain size [15]. The pinning effect of these particles restricts the dynamic recovery and retards the grain growth during dynamic recrystallization [43]. Previous investigations were done on the effect of FSP passes on the grain size [6,15,40,44]. In aluminum alloys, the grain size barely changes after various processing passes [40,44]. After the addition of second-phase particles, the situation is totally different. Huang et al. [6] reported that increasing FSP passes led to further reduction in the grain size of W/1060 Al composites. They attributed the reduction in grain size with multi-pass FSP to the more uniform distribution of W particles, which provided more nucleation sites and an effective pinning effect on the grain boundaries. Inconsistent with the result of Huang et al. [6], Ma et al. [15] reported that the average grain size of the four-pass sample was larger than that of the one-pass sample in Al-Mg-Si alloys reinforced with TiB_2 particles. In this study, the four-pass sample presented the smallest grain size while the two-pass sample had the largest grain size (Table 1). The differences in separate studies may be attributed to different matrix alloying systems. In W/1060 Al composites [6], no alloy phases but W particles have an effect on the recrystallization, while in 6xxx and 7xxx composites, the alloy phases experience a precipitation sequence during multi-pass FSP [35,45], which results in the different pinning effects of the alloy phases on the movement of grain boundaries. According to the gain-size distributions of the FSP-treated PR alloys, as shown in Figure 7d–f, the maximum grain size is about 2–3 times larger than the average. The grain size distribution deviates little when compared to the ordinary 2.5 times for an ideal grain assembly [46]. This ideal grain assembly in the FSP-treated PR alloys reveals that TiB_2 particles can enhance the homogeneity of the deformation of the Al alloy matrix [47]. The average grain sizes of the one-pass and two-pass samples are both centered at around 2 μm. The two-pass sample shows a slightly wider grain size distribution and a slightly larger average grain size than those of the one-pass sample. The four-pass PR alloy shows the narrowest grain size distribution, which reveals that the dispersion of TiB_2 particles in the matrix improves the uniformity of grain size distribution. Figure 7g–i show the misorientation angle histograms of the FSP-treated PR alloys. The misorientation distributions of multi-pass, FSP-treated samples are very close to a random grain assembly, as indicated by the black line [48]. The fraction of the HAGB is around 96% (as listed in Table 1) and very close to 97% for the random grain assembly [48]. Since boundaries with misorientation angles lower than 2° are not considered, the calculated fractions of the HAGB can be a bit higher than the actual fractions. The high proportion of HAGB in the FSP-treated PR alloys is due to the occurrence of the complete dynamic recrystallization in the nugget zone. During FSP, the high temperature and severe plastic deformation will promote the process of dynamic recrystallization [49]. Since the HAGB is more stable than the LAGB in the heat treatment, a high proportion of the HAGB may contribute to the thermal stability of the sample.

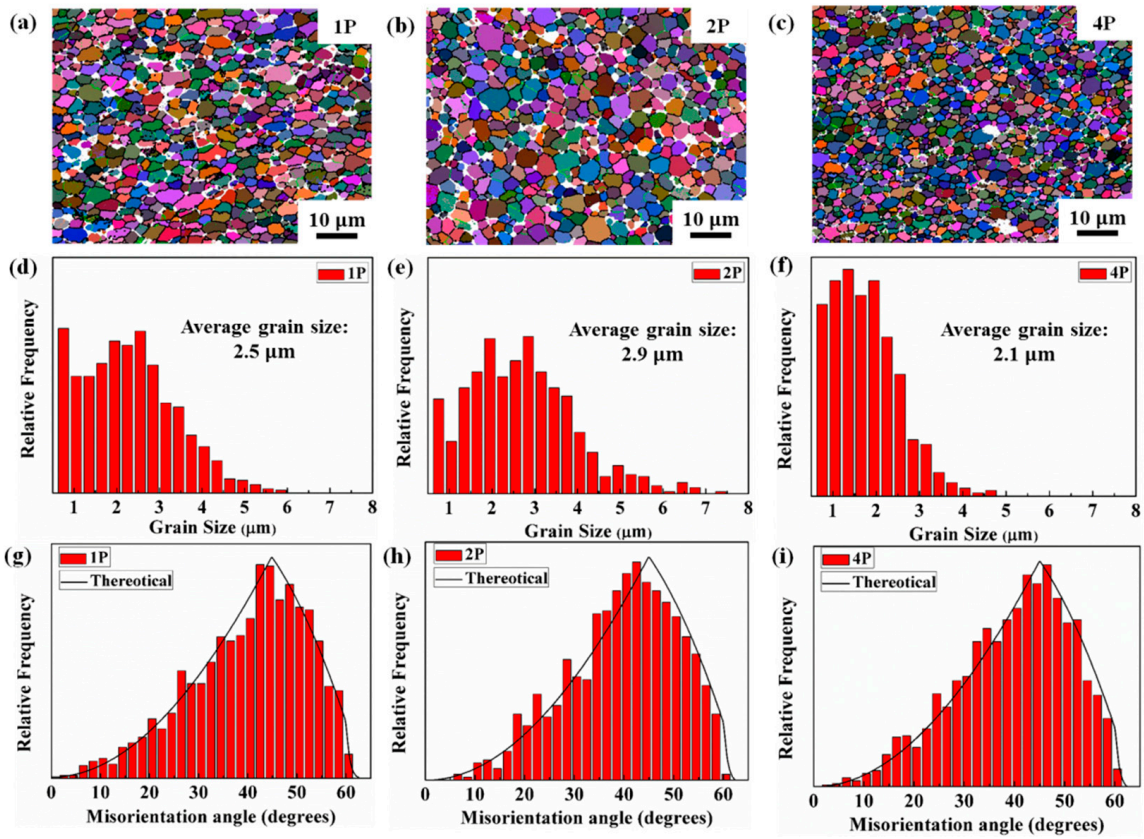

Figure 7. As-obtained orientation image microscopy (OIM) map of (**a**) 1-pass; (**b**) 2-pass; (**c**) 4-pass FSP-treated PR alloy; (**d**–**f**) corresponding grain size distribution of different passes; (**g**–**i**) corresponding misorientation distribution of different passes.

Table 1. Microstructural characteristics of the PR alloys under different processing conditions.

Material	Fraction of HAGB (%)	Average Grain Size (μm)	Average Aspect Ratio
As-cast	-	27.2	-
1-pass	95	2.5	1.50
2-pass	96	2.9	1.47
4-pass	96	2.1	1.44
1-pass-T6	95	2.7	1.28
2-pass-T6	96	2.9	1.40
4-pass-T6	96	2.8	1.45

3.3. Thermal Stability of the Microstructure

The SEM images of the FSP-treated PR alloys before and after T6 treatment are shown in Figure 8a,b, respectively. No abnormal grain growth (AGG) was observed. Table 1 also shows that the average grain sizes of the T6-treated, FSP-treated samples are in the range of 2–3 μm, which are slightly greater than those of the FSP-treated samples. The XRD patterns of the T6-treated samples with various FSP passes are presented in Figure 9, with no obvious peak of precipitates detected. Most of the precipitates are dissolved after solution treatment, and re-precipitate in fine particles during aging treatment. Since the size of reprecipitate particles is less than 10 nm, they can hardly be detected by the XRD and SEM [35]. In the FSP-treated aluminum alloys, the thermal stability of the grain structure is strongly influenced by the pinning effect of second-phase particles [46,50]. The work on Al-Zn-Mg-Sc alloys has showed that AGG occurred due to the drop in pinning forces as the precipitates dissolved at high temperature during solution treatment along with the inherent

microstructural heterogeneity in the FSP microstructure [18]. Charit et al. [51] studied FSP-treated 7475 Al alloys and proposed two strategies to avoid AGG: one was to homogenize the microstructure in the nugget zone in order to eliminate the thermodynamic driving forces generated by the grain size distribution; the other was to select alloys with a sufficient volume fraction of stable particles. Humphreys [52] proposed a theory of recrystallization which could be used to analyze the influence of second-phase particles on abnormal grain growth. Hassan et al. [19] applied Humphreys' model to AA7010 alloy and believed that a grain size of at least 10 μm in the nugget zone was required for 7xxx aluminum alloys to avoid AGG during solution treatment because of the insufficient quantity of the thermal precipitates needed for the pinning effect. In this work, the FSP-treated PR alloys with a grain size of around 2–3 μm exhibited good thermal stability during the following T6 treatment, no AGG was observed, although a high solution temperature of 475 °C was chosen. This is presumably due to the existence of thermally-stable TiB_2 particles playing an effective pinning role in the grain boundaries, thereby inhibiting the abnormal grain growth at high temperature. In addition, the multi-pass FSP improves the homogenization of the microstructure, which reduces the overall thermodynamic driving force for AGG.

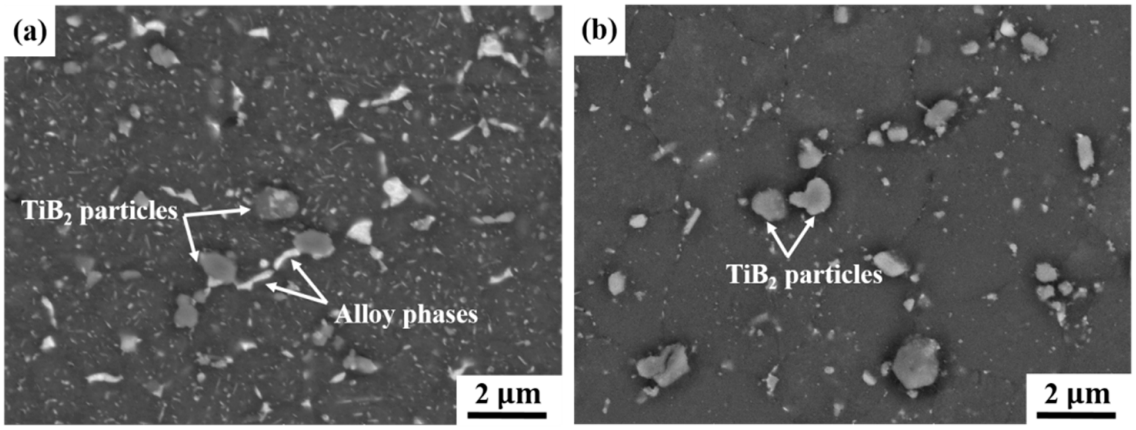

Figure 8. SEM images of (**a**) 4-pass FSP-treated sample and (**b**) T6-treated, 4-pass FSP-treated sample.

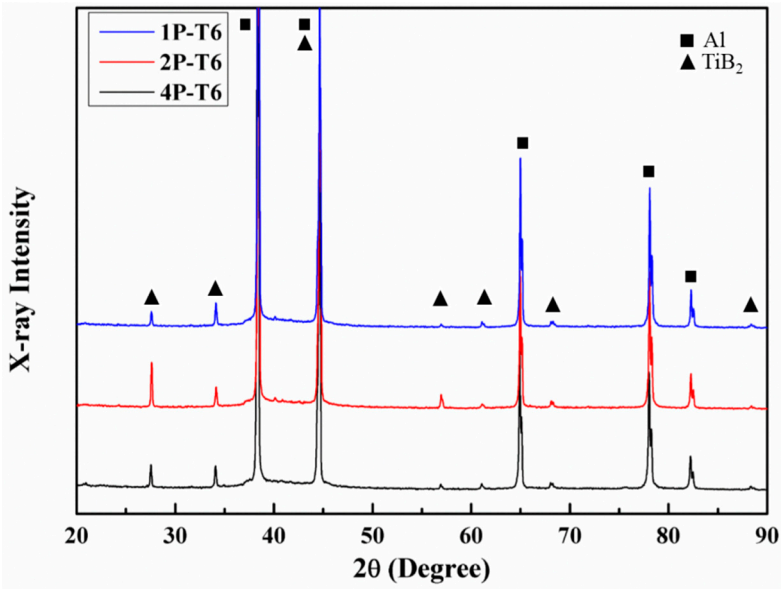

Figure 9. X-ray diffraction patterns for the T6-treated samples with various FSP passes.

3.4. Mechanical Properties

Figure 10 shows the engineering stress–strain curves of the T6-treated as-cast and FSP-treated PR alloys with different processing passes. It can be seen that the yield strength (YS) and the ultimate tensile strength (UTS) of the FSP-treated samples are far higher than those for the as-cast alloys. The best FSP condition is four-pass, where the YS is increased by 48% and the UTS by 30% compared with those of the as-cast samples. Based on the microstructure analyzed by XRD and SEM/EDS, the effective increase in strength can be attributed to the refined grains, the uniform distribution of TiB_2 particles and the increase of fine precipitates after T6 treatment. The strength is much higher than that of the FSP-treated TiB_2/AA7075 [8] and 7075 Al alloys. The specific mechanisms will be discussed in the following.

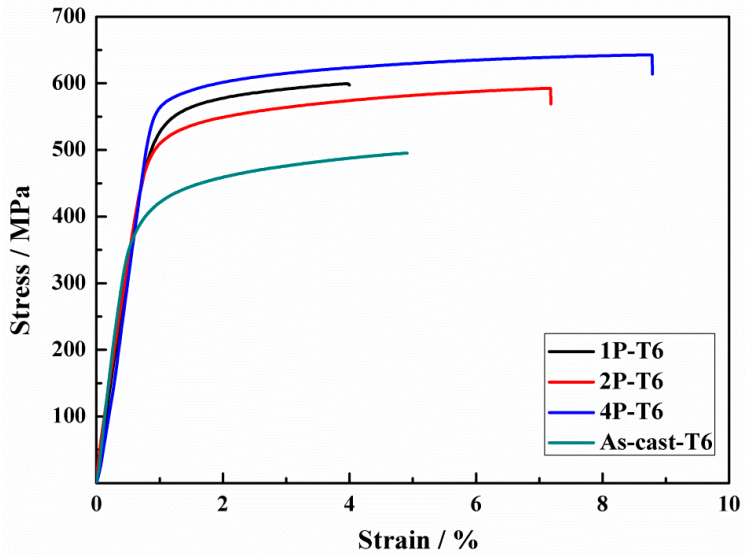

Figure 10. Stress-strain curves of T6-treated as-cast and FSP-treated PR alloys with various passes.

The fine-grained structure of the FSP-treated PR alloys is maintained after T6 treatment. According to the Hall-Petch relationship, the decrease in the average grain diameter leads to the increase in strength. Due to the previous analysis, the average grain size of the FSP-treated samples was around 2.5 μm, which is one order smaller than for the as-cast samples (around 30 μm). Therefore, it is obvious that grain refinement is one of the primary mechanisms for improving the strength of the FSP-treated samples.

The uniform distribution of TiB_2 particles plays an important role in the enhancement of strength in the FSP-treated samples. According to the Orowan strengthening mechanism, strength is inversely proportional to interparticle spacing. After FSP, the TiB_2 clusters in the as-cast samples (Figure 1) are broken up and uniformly distributed in the matrix (Figure 4). This result leads to a decrease in the interval of particles, and thus enhances the Orowan strengthening effect. As the number of processing passes increases, more uniform TiB_2 particles are obtained, which further reduces the interparticle spacing and results in the increment in the Orowan strengthening.

Not only TiB_2 particles but also precipitates like the η phase contribute to the Orowan strengthening and the strength increase due to precipitation can be written as the Equation (1) [53]:

$$\sigma_p = k\frac{f}{r}, \quad (1)$$

where r is the average diameter of precipitates and f is the volume fraction of precipitates. Apparently, increasing f and decreasing r are the two ways to enhance the strength. Since the inhibition effect of TiB_2 shells on the diffusion of alloy atoms is reduced by the dispersed TiB_2 particles, the diffusion

process is accelerated. Compared with the partial dissolution in the as-cast samples, as shown in Figure 2, the more complete solution in the FSP-treated samples leads to a larger *f*. Besides, the alloy phases go into the solution and re-precipitate in fine particles, which decreases the value of *r* [35]. Due to the larger *f* and smaller *r* of the FSP-treated samples, a higher strength is achieved than that of the as-cast ones.

Except for the one-pass samples, which exhibit a slightly lower elongation than the as-cast samples, the two-pass and four-pass samples both show a larger increase in ductility than that of the as-cast samples. This implies that FSP can improve not only the strength but also the ductility of the as-cast PR alloys. Figure 11a shows the fracture morphologies of the T6-treated, as-cast samples. It can be clearly seen that large TiB_2 clusters and alloy segregation exist on the fracture surface of the as-cast samples. This phenomenon is consistent with the TiB_2 and alloy segregation distribution shown in Figure 1. The clusters in the as-cast PR alloys will result in stress concentration and thereby promote the occurrence of porosities in the matrix nearby, as marked by arrows in Figure 11a, thus degrading ductility severely [6]. The size of dimples in the as-cast PR alloys presents bimodal distribution, in that a few alloy phases are detected in large dimples while TiB_2 particles are connected with smaller dimples. For the FSP-treated PR alloys in the T6 state, a more uniform distribution of dimples with TiB_2 particles in them is obtained and the number of porosities is decreased with the increase of the processing passes. This is due to the intense plastic strain during FSP, which modifies the distribution and size of alloy phases as well as TiB_2 particles, and eliminates porosity. A comparative observation of Figure 11e,f indicates that the dimples in the FSP-treated PR alloys are shallower than those in the as-cast alloys. Considering the second-phase particles as sites of void creation, the nucleation sites for voids will increase when the particles are dispersed. Therefore, the dimples will be created in smaller sizes and join the adjacent voids before growing to larger sizes [54]. Besides, the smaller grain size of the matrix also contributes to the shallower dimples [55]. Moreover, due to the good interfacial bonding between the dispersed TiB_2 particles and the matrix as confirmed by the presence of dimples, the ductility is enhanced with the multi-pass processing.

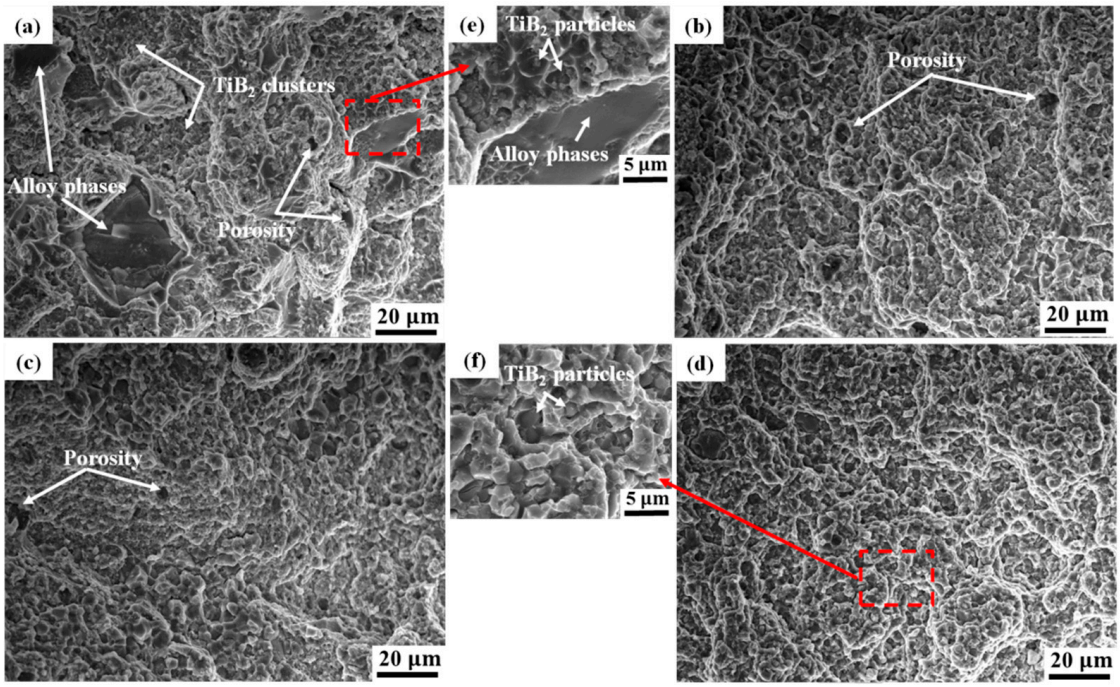

Figure 11. Tensile fractographs of (**a**) T6-treated as-cast and FSP-treated PR alloys with various passes: (**b**) 1-pass; (**c**) 2-pass; (**d**) 4-pass; (**e**) the local amplification of (**a**); (**f**) the local amplification of (**d**).

It should be noted that no necking is observed in both the as-cast and FSP-treated samples. As shown in Figure 4, FSP introduces the porosities (as marked by arrows) into the aluminum matrix, probably due to the very heterogeneous microstructures and the brittle network structure of alloy segregation and particle clustering. The fragile network structure breaks in a brittle fracture manner and cannot accommodate the plastic deformation of the matrix during the FSP, which induces the formation of porosities as the main processing defects. As the number of FSP passes increases, the fragile network structure is replaced by the dispersed second phase particles, which flow more easily during the plastic deformation. Therefore, the quantity of defects decreases in the multi-pass FSP PR alloys. Since these processing defects are probably the main reason for the fracture of the FSP-treated PR alloys, the ductility is also improved with the increase in processing passes. Technically, further work can still be done to enhance the tensile ductility by optimizing the FSP processing parameters to reduce the processing defects.

4. Conclusions

In this work, Al-Zn-Mg-Cu alloys reinforced by in-situ TiB_2 particles were successfully fabricated by FSP with various processing passes. The microstructure before and after T6 treatment were examined in terms of the grain size, the distribution of TiB_2 particles and precipitates, and their effects on the mechanical properties were evaluated. The main results are summarized as follows:

1. Multi-pass FSP improves the distribution of both TiB_2 particles and precipitates. Thus, during T6 treatment, different from the partial solution of alloy phases in the as-cast PR alloys, the diffusion process is accelerated by the dispersed TiB_2 particles in the FSP-treated PR alloys.

2. The fine grains (2–3 μm) obtained by FSP with TiB_2 particles grow slightly after T6 treatment and no abnormal grain growth was observed due to the pinning effect of TiB_2 particles.

3. The tensile strength and ductility of the PR alloys are simultaneously improved by FSP. With the increase of the FSP passes, the mechanical properties were further enhanced. The best FSP condition is four-pass, where the YS is increased by 48% and the ductility by 80% compared with that of the as-cast PR alloys.

Acknowledgments: This work is financially supported by the National Natural Science Foundation of China (Grant No. 51201099 and No. 51301108). The authors are grateful for the project 2013BB03 supported by NPL, CAEP.

Author Contributions: Zhe Chen, Yi Wu and Xiaofei Ju conceived and designed the experiments; Xiaofei Ju performed the experiments, analyzed the data and wrote the paper. Fengguo Zhang participated in the SEM and EBSD experiments and the relevant data analysis. Shengyi Zhong and Mingliang Wang participated the collection of research papers and the figure making. Gang Ji and Haowei Wang participated the revision of the manuscript. All authors had commented on the manuscript.

Conflicts of Interest: The authors declare no conflict of interest. The founding sponsors had no role in the design of the study; in the collection, analyses, or interpretation of data; in the writing of the manuscript, and in the decision to publish the results.

References

1. Li, P.; Chen, T. Tensile properties and fracture behavior of a powder-thixoformed 2024Al/SiCp composite at elevated temperatures. *Metals* **2017**, *7*, 408. [CrossRef]
2. Kim, H.J.; Lee, J.M.; Cho, Y.H.; Kim, J.J.; Kim, S.H.; Lee, J.C. Effects of processing parameters on the fabrication of in-situ Al/TiC composites by thermally activated combustion reaction process in an aluminium melt using Al-TiO_2-C powder mixtures. *J. Korean Inst. Met. Mater.* **2012**, *50*, 677–684.
3. Liu, G.; Zhang, G.J.; Jiang, F.; Ding, X.D.; Sun, Y.J.; Sun, J.; Ma, E. Nanostructured high-strength molybdenum alloys with unprecedented tensile ductility. *Nat. Mater.* **2013**, *12*, 344–350. [CrossRef] [PubMed]
4. Chen, L.Y.; Xu, J.Q.; Choi, H.; Pozuelo, M.; Ma, X.; Bhowmick, S.; Yang, J.-M.; Mathaudhu, S.; Li, X.-C. Processing and properties of magnesium containing a dense uniform dispersion of nanoparticles. *Nature* **2015**, *528*, 539–543. [CrossRef] [PubMed]

5. Zhang, W.; Hu, Y.; Zhang, G.; Wang, Z. Formation of nanoscale metallic glassy particle reinforced Al-based composite powders by high-energy milling. *Metals* **2017**, *7*, 425. [CrossRef]
6. Huang, G.; Shen, Y.; Guo, R.; Guan, W. Fabrication of tungsten particles reinforced aluminum matrix composites using multi-pass friction stir processing: Evaluation of microstructural, mechanical and electrical behavior. *Mater. Sci. Eng. A* **2016**, *674*, 504–513. [CrossRef]
7. Suryanarayana, C.; Al-Aqeeli, N. Mechanically alloyed nanocomposites. *Prog. Mater. Sci.* **2013**, *58*, 383–502. [CrossRef]
8. Rajan, H.B.M.; Dinaharan, I.; Ramabalan, S.; Akinlabi, E.T. Influence of friction stir processing on microstructure and properties of AA7075/TiB_2 in situ composite. *J. Alloys Compd.* **2016**, *657*, 250–260. [CrossRef]
9. Wang, M.; Chen, D.; Chen, Z.; Wu, Y.; Wang, F.; Ma, N.; Wang, H. Mechanical properties of in-situ TiB_2/A356 composites. *Mater. Sci. Eng. A* **2014**, *590*, 246–254. [CrossRef]
10. Hong, T.; Li, X.; Wang, H.; Chen, D. Influence of solution temperature on microstructure and properties of in-situ TiB_2/2009 composites. *Mater. Sci. Eng. A* **2015**, *634*, 1–4. [CrossRef]
11. Geng, J.; Hong, T.; Ma, Y.; Wang, M.; Chen, D.; Ma, N.; Wang, H. The solution treatment of in-situ sub-micron TiB_2/2024 Al composite. *Mater. Des.* **2016**, *98*, 186–193. [CrossRef]
12. Mishra, R.S.; Ma, Z.Y. Friction stir welding and processing. *Mater. Sci. Eng. R* **2005**, *50*, 1–78. [CrossRef]
13. Chen, X.G.; da Silva, M.; Gougeon, P.; St-Georges, L. Microstructure and mechanical properties of friction stir welded AA6063–B4C metal matrix composites. *Mater. Sci. Eng. A* **2009**, *518*, 174–184. [CrossRef]
14. Morisada, Y.; Fujii, H.; Nagaoka, T.; Fukusumi, M. Effect of friction stir processing with SiC particles on microstructure and hardness of AZ31. *Mater. Sci. Eng. A* **2006**, *433*, 50–54. [CrossRef]
15. Ma, S.M.; Zhang, P.; Ji, G.; Chen, Z.; Sun, G.A.; Zhong, S.Y.; Ji, V.; Wang, H.W. Microstructure and mechanical properties of friction stir processed Al–Mg–Si alloys dispersion-strengthened by nanosized TiB_2 particles. *J. Alloys Compd.* **2014**, *616*, 128–136. [CrossRef]
16. Du, Z.; Tan, M.J.; Guo, J.F.; Bi, G.; Wei, J. Fabrication of a new Al-Al_2O_3-CNTs composite using friction stir processing (FSP). *Mater. Sci. Eng. A* **2016**, *667*, 125–131. [CrossRef]
17. Carlone, P.; Astarita, A.; Rubino, F.; Pasquino, N. Microstructural Aspects in FSW and TIG Welding of Cast ZE41AMagnesium Alloy. *Metall. Mater. Trans. B* **2016**, *47*, 1340–1346. [CrossRef]
18. Charit, I.; Mishra, R.S. Low temperature superplasticity in a friction-stir-processed ultrafine grained Al–Zn–Mg–Sc alloy. *Acta Mater.* **2005**, *53*, 4211–4223. [CrossRef]
19. Hassan, K.A.A.; Norman, A.F.; Price, D.A.; Prangnell, P.B. Stability of nugget zone grain structures in high strength Al-alloy friction stir welds during solution treatment. *Acta Mater.* **2003**, *51*, 1923–1936. [CrossRef]
20. Luo, C.; Dong, F.; Guo, L. Study on Heat Treatment of Aerospace Aluminum Alloy Welded FSW. *MATEC Web Conf.* **2017**, *114*, 03010. [CrossRef]
21. Nikoo, M.F.; Azizi, H.; Parvin, N.; Naghibi, H.Y. The influence of heat treatment on microstructure and wear properties of friction stir welded AA6061-T6/Al_2O_3 nanocomposite joint at four different traveling speed. *J. Manuf. Processes* **2016**, *22*, 90–98. [CrossRef]
22. Moradi, M.M.; Aval, H.J.; Jamaati, R. Effect of pre and post welding heat treatment in SiC-fortified dissimilar AA6061-AA2024 FSW butt joint. *J. Manuf. Process.* **2017**, *30*, 97–105. [CrossRef]
23. Cui, G.R.; Ma, Z.Y.; Li, S.X. The origin of non-uniform microstructure and its effects on the mechanical properties of a friction stir processed Al–Mg alloy. *Acta Mater.* **2009**, *57*, 5718–5729. [CrossRef]
24. Peel, M.; Steuwer, A.; Preuss, M.; Withers, P.J. Microstructure, mechanical properties and residual stresses as a function of welding speed in aluminium AA5083 friction stir welds. *Acta Mater.* **2003**, *51*, 4791–4801. [CrossRef]
25. Rhodes, C. Fine-grain evolution in friction-stir processed 7050 aluminum. *Scr. Mater.* **2003**, *48*, 1451–1455. [CrossRef]
26. Charit, I.; Mishra, R.S. Abnormal grain growth in friction stir processed alloys. *Scr. Mater.* **2008**, *58*, 367–371. [CrossRef]
27. Chen, Z.; Sun, G.; Wu, Y.; Mathon, M.; Borbely, A.; Chen, D.; Ji, G.; Wang, M.; Zhong, S.; Wang, H. Multi-scale study of microstructure evolution in hot extruded nano-sized TiB_2 particle reinforced aluminum composites. *Mater. Des.* **2017**, *116*, 577–590. [CrossRef]

28. Tang, Y.; Chen, Z.; Borbély, A.; Ji, G.; Zhong, S.Y.; Schryvers, D.; Ji, V.; Wang, H.W. Quantitative study of particle size distribution in an in-situ grown Al–TiB_2 composite by synchrotron X-ray diffraction and electron microscopy. *Mater. Charact.* **2015**, *102*, 131–136. [CrossRef]
29. Schaffer, P.L.; Miller, D.N.; Dahle, A.K. Crystallography of engulfed and pushed TiB_2 particles in aluminium. *Scr. Mater.* **2007**, *57*, 1129–1132. [CrossRef]
30. Deng, Y.; Yin, Z.; Cong, F. Intermetallic phase evolution of 7050 aluminum alloy during homogenization. *Intermetallics* **2012**, *26*, 114–121. [CrossRef]
31. Mondal, C.; Mukhopadhyay, A.K. On the nature of T($Al_2Mg_3Zn_3$) and S(Al_2CuMg) phases present in as-cast and annealed 7055 aluminum alloy. *Mater. Sci. Eng. A* **2005**, *391*, 367–376. [CrossRef]
32. Cong, F.; Zhao, G.; Jiang, F.; Tian, N.; Li, R. Effect of homogenization treatment on microstructure and mechanical properties of DC cast 7X50 aluminum alloy. *Nonferrous Met. Soc. China* **2015**, *25*, 1027–1034. [CrossRef]
33. Li, X.M.; Starink, M.J. Effect of compositional variations on characteristics of coarse intermetallic particles in overaged 7000 aluminium alloys. *Mater. Sci. Technol.* **2001**, *17*, 1324–1328. [CrossRef]
34. Li, Y.Y.; Kovarik, L.; Phillips, P.J.; Hsu, Y.F.; Wang, W.H.; Mills, M.J. High resolution characterization of the precipitation behavior of an Al-Zn-Mg-Cu alloy. *Philos. Mag. Lett.* **2012**, *92*, 166–178. [CrossRef]
35. Su, J.Q.; Nelson, T.W.; Mishra, R.; Mahoney, M. Microstructural investigation of friction stir welded 7050-T651 aluminium. *Acta Mater.* **2003**, *51*, 713–729. [CrossRef]
36. Zhang, Z.; Yang, R.; Guo, Y.; Chen, G.; Lei, Y.; Cheng, Y.; Yue, Y. Microstructural evolution and mechanical properties of ZrB2/6061Al nanocomposites processed by multi-pass friction stir processing. *Mater. Sci. Eng. A* **2017**, *689*, 411–418. [CrossRef]
37. Prater, T. Solid-state joining of metal matrix composites: A survey of challenges and potential solutions. *Mater. Manuf. Process.* **2011**, *26*, 636–648. [CrossRef]
38. Rhodes, C.G.; Mahoney, M.W.; Bingel, W.H.; Spurling, R.A.; Bampton, C.C. Effects of friction stir welding on microstructure of 7075 aluminum. *Scr. Mater.* **1997**, *36*, 69–75. [CrossRef]
39. Li, H.; Cao, F.; Guo, S.; Ning, Z.; Liu, Z.; Jia, Y.; Scudino, S.; Gemming, T.; Sun, J. Microstructures and properties evolution of spray-deposited Al-Zn-Mg-Cu-Zr alloys with scandium addition. *J. Alloys Compd.* **2017**, *691*, 482–488. [CrossRef]
40. Johannes, L.B.; Mishra, R.S. Multiple passes of friction stir processing for the creation of superplastic 7075 aluminum. *Mater. Sci. Eng. A* **2007**, *464*, 255–260. [CrossRef]
41. Ma, Z.Y.; Pilchak, A.L.; Juhas, M.C.; Williams, J.C. Microstructural refinement and property enhancement of cast light alloys via friction stir processing. *Scr. Mater.* **2008**, *58*, 361–366. [CrossRef]
42. McNelley, T.R.; Swaminathan, S.; Su, J.Q. Recrystallization mechanisms during friction stir welding/processing of aluminum alloys. *Scr. Mater.* **2008**, *58*, 349–354. [CrossRef]
43. Shafiei-Zarghani, A.; Kashani-Bozorg, S.F.; Zarei-Hanzaki, A. Microstructures and mechanical properties of Al/Al_2O_3 surface nano-composite layer produced by friction stir processing. *Mater. Sci. Eng. A* **2009**, *500*, 84–91. [CrossRef]
44. Ma, Z.Y.; Mishra, R.S.; Liu, F.C. Superplastic behavior of micro-regions in two-pass friction stir processed 7075Al alloy. *Mater. Sci. Eng. A* **2009**, *505*, 70–78. [CrossRef]
45. Lang, P.; Povoden-Karadeniz, E.; Falahati, A.; Kozeschnik, E. Simulation of the effect of composition on the precipitation in 6xxx Al alloys during continuous-heating DSC. *J. Alloys Compd.* **2014**, *612*, 443–449. [CrossRef]
46. Rollett, A.; Humphreys, F.; Rohrer, G.S.; Hatherly, M. *Recrystallization and Related Annealing Phenomena*, 2nd ed.; Elsevier Ltd.: Oxford, UK, 2004; pp. 248–249.
47. Chen, Z.; Li, J.; Borbely, A.; Ji, G.; Zhong, S.Y.; Wu, Y.; Wang, M.L.; Wang, H.W. The effects of nanosized particles on microstructural evolution of an in-situ TiB_2/6063Al composite produced by friction stir processing. *Mater. Des.* **2015**, *88*, 999–1007. [CrossRef]
48. Mackenzie, J. Second paper on statistics associated with the random disorientation of cubes. *Biometrika* **1958**, *45*, 229–240. [CrossRef]
49. Liu, F.C.; Ma, Z.Y. Contribution of grain boundary sliding in low-temperature superplasticity of ultrafine-grained aluminum alloys. *Scr. Mater.* **2010**, *62*, 125–128. [CrossRef]
50. Mahoney, M.; Rhodes, C.; Flintoff, J.; Bingel, W.; Spurling, R. Properties of friction-stir-welded 7075 T651 aluminum. *Metall. Mater. Trans. A* **1998**, *29*, 1955–1964. [CrossRef]

51. Charit, I.; Mishra, R.S.; Mahoney, M.W. Multi-sheet structures in 7475 aluminum by friction stir welding in concert with post-weld superplastic forming. *Scr. Mater.* **2002**, *47*, 631–636. [CrossRef]
52. Humphreys, F. A unified theory of recovery, recrystallization and grain growth, based on the stability and growth of cellular microstructures—II. The effect of second-phase particles. *Acta Mater.* **1997**, *45*, 5031–5039. [CrossRef]
53. Cheng, S.; Zhao, Y.H.; Zhu, Y.T.; Ma, E. Optimizing the strength and ductility of fine structured 2024 Al alloy by nano-precipitation. *Acta Mater.* **2007**, *55*, 5822–5832. [CrossRef]
54. Barmouz, M.; Givi, M.K.B.; Seyfi, J. On the role of processing parameters in producing Cu/SiC metal matrix composites via friction stir processing: Investigating microstructure, microhardness, wear and tensile behavior. *Mater. Charact.* **2011**, *62*, 108–117. [CrossRef]
55. Guo, J.; Chen, H.; Sun, C.; Bi, G.; Sun, Z.; Wei, J. Friction stir welding of dissimilar materials between AA6061 and AA7075 Al alloys effects of process parameters. *Mater. Des.* **2014**, *56*, 185–192. [CrossRef]